THERMAL ANALYSIS AND OPTIMIZATION OF A SUPERCRITICAL CO2 BRAYTON CYCLE CONNECTED TO A CENTRAL TOWER SOLAR COLLECTOR.

J.A. Moctezuma-Hernandez[1]*, Judit García-Ferrero[1], Rosa. P. Merchán[1], J.M.M. Roco[1]

[1]Universidad de Salamanca, Departamento de Física Aplicada, Salamanca, Spain.

*Corresponding Author: ja.moctezuma@usal.es

ABSTRACT

A thermodynamic model of a Concentrated Solar Power (CSP) plant for both solar radiation collection system and the thermal conversion is presented. The radiation collection process in the CSP is performed by a central tower system, which uses a fluidized bed of silicon carbide and air a heat transfer system. The energy transfer process in the central tower system is set at a temperature of 650°C for the fluidized bed at the exit of the tower and modeled a heat transfer coefficient of $411 W/m^2K$. The CSP plant uses a hybrid Brayton cycle of supercritical CO_2 connected to the central tower system, which is modeled and validated by an air Brayton cycle that reproduces the behavior of a real plant under design conditions. The conversion of heat into work is optimized by maximizing the thermal efficiency and minimizing the fuel consumption of the auxiliary support system. The results of the optimization process predict an increase in the thermal efficiency of 13.3% and a decrease of 58.8% in the fuel mass flow.

1 INTRODUCTION

The use of solar energy for power generation has acquired significant relevance due to its renewable nature and potential for reducing carbon emissions. In this sense, in recent decades there has been a growing interest in concentrating solar power plants (CSP), especially in solar power towers, where the solar radiation captured by a heliostat farm is concentrated in a receiver, which can be a particle receiver. Inside this solar receiver, a heat transfer fluid is used to increase its temperature to values above 500°C [1]. This heat transfer fluid can be integrated into a power system, either a Rankine or Brayton cycle, for electric power generation.

The use of a fluidized bed of air and solid particles as heat fluid transfer has been revealed as a promising way to improve the energy collection of solar radiation. For this purpose, an effective heat transfer fluid inside the particle receiver is key to reaching high temperatures. In this line, Perez-Lopez *et al*. [2] experimented with a solar receiver with a dense particle suspension (DPS), where the particles were silicon carbide (SiC) with a volume fraction of 30%. Sixteen tubes were used. The tests were performed with a mass flow variation of 660-1760 kg/h, and a solar thermal power of 60-142 kW. The results showed a DPS outlet temperature of 700°C, as well as a receiver efficiency between 50% and 90%. Another important advantage of using a dense particulate or fluidized bed solution over other heat transfer fluids, such as molten salts, is its operating and maintenance costs. Zhang *et al*. [3] performed an analysis of the efficiency, capital, and operating cost of a concentrating solar tower system using DPS as the heat transfer fluid inside the receiver. They employed a 1MW thermal power furnace, resulting in a convective coefficient of 1100 and 2200 W/m^2K, for a gas velocity of 0.04 to 0.19 m/s. The levelized cost of electricity (LCOE) could have a decrease between 10% and 20% compared to the use of molten salts. This reduction has been ascribed to a decrease in pumping energy, an absence of thermal looping, and a reduction in the thermal output of the heliostat array. An important aspect of the particle receiver is the modeling of heat transfer. In this regard, Wang *et al*. [4] developed a model in

https://doi.org/10.52202/077185-0129

computational fluid dynamics (CFD) software, using a fluidized bed as the heat transfer fluid. The model was performed in 2D, considering the particle velocity and diameter. The results showed that these two parameters have a greater influence on heat transfer by convection than by conduction, determining that particle-fluid convection dominates in heat transfer, whereas particle-particle conduction is negligible.

On the other hand, in recent years, supercritical carbon dioxide (sCO_2) cycles have attracted great interest in their coupling with concentrating solar power plants because they have proven to be more compact, safer, and economically more profitable [5], [6]. Another positive aspect of using CO_2 is that its critical pressure is high (7.37 MPa), besides being non-toxic and non-flammable [7]. When CO_2 works at conditions very close to its critical point, it turns very dense, which requires very little compression work. By having low compression work and high temperatures within the cycle, higher thermodynamic efficiencies are obtained than in a conventional Rankine cycle [8]. For this reason, Khatoon and Kim [9] performed an analysis of a Brayton cycle with supercritical carbon dioxide using a solar concentrating plant. They performed the analysis with two direct normal radiation, 1700 and 1300 kWh/m^2. Inside the particle receiver, they used molten salts as heat transfer fluid. The results show that the best efficiency is achieved with the coupled recompression cycle system. The calculated net power is 37.17 and 39.07 MW, with regenerative and recompression cycles, respectively. Furthermore, Guelpa and Verda [10], performed an exergoeconomic analysis of a Brayton cycle with sCO_2 coupled to a concentrating solar power plant. By combining economic and exergy-economic analysis in an energy system, it can be observed where the system experiences the highest irreversibilities and malfunctions. The exergoeconomic indicators showed the need for a redesign to obtain a better performance in the design parameters of the system.

In this work, an analysis of a hybrid Brayton cycle with sCO_2 is performed. The power system is coupled to a concentrating solar power plant, specifically to a central receiver using a fluid of particles and air as a heat transfer system. The particle receiver is modeled to first understand and reproduce how the heat transfer process is carried out. A heat transfer fluid used is a fluidized bed, in particular a combination of silicon carbide particles and air. The outlet temperature of the particle receiver is set to 650°C. Then coupled power cycle is optimized to maximize thermal efficiency and minimize fuel mass flow. The decision variables of the optimization process will be the inlet temperature and pressure of the compression process, the compression ratio, the mass flow of CO_2, and the inlet temperature to the turbine. NSGA-II algorithm is used to perform this optimization providing optimum values of input parameters. Promising results in the optimal regime about increasing the thermal efficiency of the energy conversion and reducing fuel mass consumption of the hybrid system are obtained.

2 MODELING

Modeling of the particle receiver system and heat transfer between the heliostat field radiation and the fluidized bed presented in this work is based on the works done by Gallo *et al*. [11] and Córcoles *et al*. [12], respectively. On the other hand, the modeling of the power cycle performance is described by energy and mass balances in each component. The software used to model the system is Mathematica [13].

2.1 Particle Receiver

A mixture of two fluids, silicon carbide, and air, circulates inside the particle receiver. The calculation of the thermodynamic properties of this fluid mixture (fluidized bed) is presented below. Table 1 shows some values of the properties of silicon carbide. All thermodynamic properties were evaluated using the mean temperature. In Eqs. (1)-(3), the mass flow per unit area of the fluidized bed (G_{DPS}) and specific heat of the fluidized bed ($C_{p,DPS}$), are calculated [11].

$$G_{DPS} = \varphi_p \rho_p (u_g - u_{mf}) + (1 - \varphi_p) \rho_g u_g \tag{1}$$

https://doi.org/10.52202/077185-0129

$$\rho_{DPS} = \varphi_p \rho_p + (1 - \varphi_p)\rho_g \tag{2}$$

$$C_{p,DPS} = \frac{\varphi_p \rho_p C_{p,p} + (1 - \rho_p)\rho_g C_{p,g}}{\varphi_p \rho_p + (1 - \varphi_p)\rho_g} \tag{3}$$

These equations are expressed in terms of the volumetric fraction of particle suspension, φ_p; the gas velocity, u_g; the minimum fluidization velocity, u_{mf}; and the specific heat of the particle and gas $C_{p,p}, C_{p,g}$, respectively.

Table 1. Properties of silicon carbide [14]

Property	Units	Value
Sauter mean diameter (d_p)	[μm]	63.9
Density (ρ_p)	$[kg\ m^{-3}]$	3210
Thermal conductivity (at 500°C)	$[\mathrm{W}m^{-1}K^{-1}]$	109
Minimum fluidization velocity (u_{mf})	$[mm/s]$	5.5

Once the thermodynamic properties are known, the mass flow rate of the fluidized bed ($\dot{m}_{DPS}$) can be calculated. This flow rate is the sum of the particle and gas mass flow rates, ($\dot{m}_p, \dot{m}_g$, respectively). By performing an energy balance inside the particle receiver, these variables can be calculated as seen in Eqs. (4) and (5), where $\dot{Q}_{rec}$ is the thermal power delivered to the receiver by the heliostat field, in this work it takes a $\dot{Q}_{rec} = 57\ MW$. $\dot{Q}_{losses}$ are calculated considering the heat losses by radiation and convection from the tube to the environment. Calculated heat losses $\dot{Q}_{rec}$ is updated. The outlet temperature of the particle receiver is set to $T_p^{out} = 650\ °C$. This analysis was carried out iteratively since the inlet temperature of the particles in the receiver (T_p^{in}) is proposed at the beginning of the calculation. The convergence criterion is to analyze the thermodynamic properties of the past iteration with the current one, if the difference is less than 0.01 the iterative process ends. This process is shown in Figure 1.

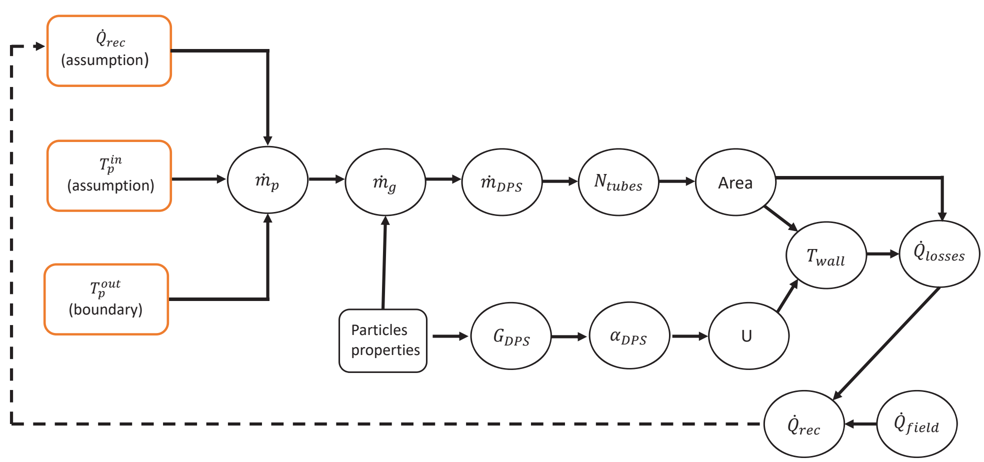

Figure 1. Iterative process for particle receiver modeling

https://doi.org/10.52202/077185-0129

$$\dot{m}_p = \frac{\dot{Q}_{rec}}{C_{p,p}(T_p^{out} - T_p^{in})} \tag{4}$$

$$\dot{m}_g = \frac{(1-\varphi_p)\rho_p u_g}{\varphi_p \rho_p (u_g - u_{mf})} \dot{m}_p \tag{5}$$

Next, the calculation of the number of tubes (N_{tubes}) necessary to reach the set temperature at the receiver outlet is made in Eq. (6), where d_i is the internal diameter of the tube.

$$N_{tubes} = \frac{4\dot{m}_{DPS}}{\pi d_i^2 G_{DPS}} \tag{6}$$

2.1.1 Heat transfer analysis

Developing a model that describes the heat transfer process inside the particle receiver is complex. The energy transfer process starts with the incidence of solar radiation from the heliostat field on the tubes. This radiation heats the tube wall and increases its temperature, allowing in turn to heat the fluidized bed by convection and conduction, who's particles gain a higher temperature. This energy transfer process can be seen graphically in Figure 2.

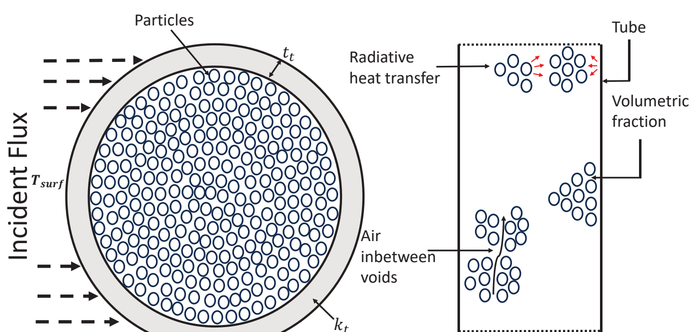

Figure 2. Heat transfer process inside the receiver.

This whole process of energy transfer is described through the global coefficient of heat transfer (U), which is shown in Eq (7) [11]. This equation is obtained from the analysis of the global coefficient for cylindrical coordinates.

$$U = f_{act}\alpha_{DPS} + 2\frac{\sqrt{\alpha_{DPS}k_t t_t}}{\pi d_i} tanh\left[\pi\left(d_i + \frac{t_t}{2}\right)\left(\frac{1-f_{act}}{2}\right)\sqrt{\frac{\alpha_{DPS}}{k_t t_t}}\right] \tag{7}$$

Where f_{act} is the active front fraction of the tube, which only considers the part where the solar radiation is impacting the tube, as shown in Figure 2. t_t is the thickness of the tube and α_{DPS} is the convective heat transfer coefficient. This last coefficient is of special interest because it is responsible for modeling the energy transfer inside the particle receiver. To obtain the convective coefficient of the fluidized bed, the correlations used come from the work developed by Gallo *et al.* [11]. The way to perform this analysis can be empirical or semi-empirical, in this work semi-empirical correlations were used. Eq (8) shows the computation of the heat transfer coefficient, involving the convective coefficient (α_{DPS}), which only contributes 70% to the total heat transfer coefficient [15]. On the other hand, the radiative heat transfer between particles and tube can be evaluated by Eq (9), where ε_p , ε_t are the emissivity of

https://doi.org/10.52202/077185-0129

the particle and tube, respectively. T_{mean} is the mean bed temperature and σ is the Stefan Boltzmann constant.

$$\alpha_{DPS} = 0.7\alpha_w + \alpha_{rad} \tag{8}$$

$$\alpha_{rad} = 7.3(\varepsilon_p \varepsilon_t \sigma T_{mean}^3) \tag{9}$$

The evaluation of α_{DPS} from Eq. (8), needs in turn the evaluation α_w, which can be performed by using the semi-empirical relations, Eqs. (10)-(13), proposed in the work of Córcoles *et al.* [12]. In Eqs (10)-(11), α_g is the contribution of the gas heat transfer and α_p the one of the particle's heat transfer. f_p is the coefficient of the particle volume fraction at the wall, which depends on the particle volume fraction (φ_p) and the cell volume fraction (φ_{cp}). Finally, α_{gp} refers to the heat transfer contribution between gas and particle interaction.

$$\alpha_w = \alpha_g + f_p\alpha_p + \alpha_{gp} \tag{10}$$

$$f_p = 1 - e^{-10\left(\varphi_p/\varphi_{cp}\right)} \tag{11}$$

$$\alpha_g = (c_0 Re_L^{n1} P_r^{n2} + c_1)\frac{k_g}{L} + c_2 \tag{12}$$

$$\alpha_p = \left(c_3 Re_p^{n3}\right)\frac{k_g}{d_p} \tag{13}$$

In Eqs (12)-(13), R_e is the Reynolds number, L is the length of the cell, P_r is the Prandtl number and d_p is particle diameter. c_0, c_1, c_2, c_3 are coefficients that have values of 0.46, 3.66, 0, and 0.525 W/m^2K respectively. Also, n_1, n_2, and n_3 are other coefficients whose values are 0.5, 0.33, and 0.75, respectively. The values of these coefficients were obtained from previous works [16], [17]. The heat transfer between the fluid phase and the particle phase is modeled with the fluid-particle heat transfer coefficient (α_{gp}) that is defined in Eq (14). Where c_4, c_5, c_6, n_4, and n_5 are coefficients that have values of 0.37, 0.1, 0 W/m^2K , and 0.6, 0.33 respectively. These data fit correctly with experimental data [6].

$$\alpha_{gp} = (c_4 Re^{n_4} P_r^{n_5} + c_5)\frac{k_g}{d_p} + c_6 \tag{14}$$

2.2 Power block

The past description of the heat transfer process inside the solar collector allows to know the fluidized bed outlet temperature. Hence, the Brayton cycle with sCO_2 as a working fluid can be modeled next. Figure 3 shows the scheme of the cycle under analysis, each color represents the working fluid used in each section. sCO_2 enters the compressor with a temperature T_1, then it is compressed until reaching a pressure P_2 and a temperature T_2.

The system has a heat recuperator, in which the fluid from the turbine outlet enters at a temperature T_4. On the other hand, the fluid from the compressor outlet enters this heat recuperator and exits it at a T_x

https://doi.org/10.52202/077185-0129

temperature. Next, a new heat input from the solar receiver is added. This occurs in heat exchanger number one (HEX-1), where the fluidized bed of the solar receiver enters the exchanger and transfers energy in the form of heat to the sCO_2, which exits at a temperature T_z. Finally, the energy supply through the combustion of natural gas takes place in the heat exchanger number two (HEX-2). The working fluid achieves the desired temperature T_3, entering the gas turbine, where an expansion takes place, and the turbine produces work.

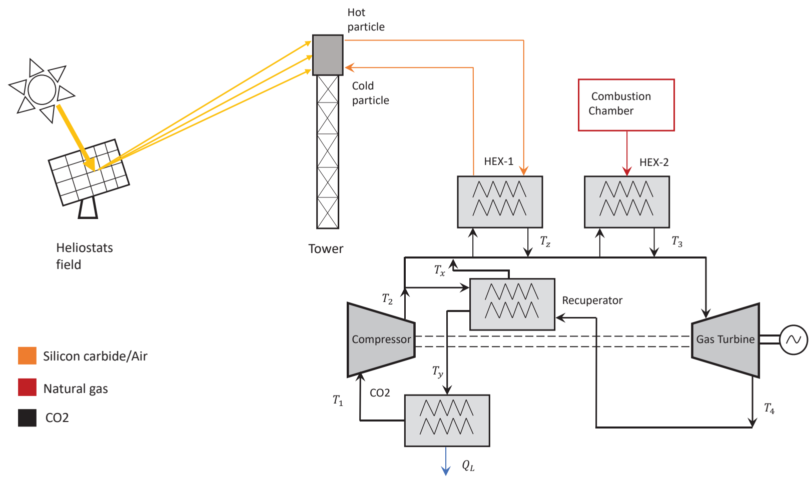

Figure 3. Schematic of the power cycle coupled to the particle receiver.

2.2.1 Power Cycle Model (Brayton Cycle)

Performing an energy balance at the compressor and gas turbine, the following two equations are obtained:

$$\left|\dot{W}_{comp}\right| = \dot{m}(h_2 - h_1) \tag{15}$$

$$\left|\dot{W}_{GT}\right| = \dot{m}(h_3 - h_4) \tag{16}$$

Where $\dot{m}$ is the mass flow rate of the CO_2 cycle and h is the enthalpy in each thermodynamic state. Continuing with the analysis, it is the turn of the heat exchangers, whose main function is to transfer energy in the form of heat between two fluids. How both the recuperator and the HEX-1 exchanger were analyzed are described in Eqs (17)-(18), respectively.

$$\left|\dot{Q}_{recu}\right| = \epsilon_{recu}\left|\dot{Q}_{2-x}\right| \tag{17}$$

$$\left|\dot{Q}_{HS}\right| = \epsilon_{HS}\left|\dot{Q}_{x-z}\right| \tag{18}$$

Where $\dot{Q}_{recu}$ represents the heat transferred from the flow leaving the gas turbine, while $\dot{Q}_{2-x}$ represents the heat absorbed by the flow leaving the compressor. From this equation the temperature T_x can be known. On the other hand, $\dot{Q}_{HS}$ is the heat contributed by the solar receiver. From this analysis the temperature T_z can be known. ϵ_{rec} and ϵ_{HC} are the effectivenesses of the heat exchanger: for this work

https://doi.org/10.52202/077185-0129

values of 0.775 and 0.98 [18] were used, respectively. ϵ_{HS} has a value 0.78. On the other hand, combustion is performed before HEX-2, hence a different equation is employed [18]:

$$\left|\dot{Q}_{HC}\right| = \epsilon_{HC}\left|\dot{Q}_{z-3}\right| = \epsilon_{HC}\eta_c\dot{m}_f Q_{LHV} \qquad (19)$$

Where η_c is the combustion efficiency. In this work, natural gas is used. The waste heat of the system ($\dot{Q}_L$) can be calculated using Eq (20). This waste heat can be used for processes where an energy supply is required, either hot water or a cogeneration cycle. Finally, $\dot{Q}_h$ is the total heat input to the cycle, which is defined as the sum of the receiver heat and the combustion chamber heat ($\dot{Q}_h = \dot{Q}_{HS} + \dot{Q}_{HC}$).

$$\left|\dot{Q}_L\right| = \dot{m}(h_y - h_1) \qquad (20)$$

3 VALIDATION

3.1 Particle receiver validation

The geometrical and heat transfer data are compared with what is reported in the literature. The work of Belmonte *et al.* [14] was taken as a reference, since in this work they perform the same geometrical analysis performed by Gallo *et al.* [11]. Table 2 shows the relative error ranging from 2% to 11%. This maximum relative error of 11% corresponds to the computation of the absorption area, where the error propagates resulting in the highest error among the analyzed variables. Nonetheless, the behavior of the particle receiver model shows a good agreement.

Table 2. Comparison of present work concerning the literature.

Properties	Present work	Belmonte *et al.* [14]	Relative error (%)
Convective coefficient $\boldsymbol{\alpha_{DPS}\,[Wm^{-2}K^{-1}]}$	411	430-750	4.4
Particle mass flow $\boldsymbol{[Kgs^{-1}]}$	117.84	121.9	3.3
Number of tubes [-]	388	396	2.0
Absorption area $\boldsymbol{[m^2]}$	127	143	11

3.2 Power cycle validation

For the validation of the power cycle, the TRNSYS 18 software was used [19]. This software is employed due to its capacity to perform transient and dynamic analysis, as well as to make connections with other programs, such as the EES software [20]. The connection with EES occurs because the particle receiver has been programmed also in this language (apart from Mathematica). The database REFPROP is used for the thermodynamic properties to model the system. The simulation in TRNSYS is shown in Figure 4. In the simulation, the working fluid in the power cycle is air. This fluid is selected because TRNSYS does not handle the thermodynamic properties of other fluids. Therefore, within the model developed in Mathematica, air is also used as the working fluid and the comparison is made. The results are presented in Table 3. The comparison in Table 3 shows a low relative error in the temperatures. Thermal efficiency predicted by Mathematica code is 7% lower than TRNSYS one. As comparing Mathematica-TRNSYS simulations all relative errors are less than 10%, and the power cycle model is considered as validated. Thus, developed code can give a good prediction of what happens when changing either the working fluid or the input conditions of the system.

https://doi.org/10.52202/077185-0129

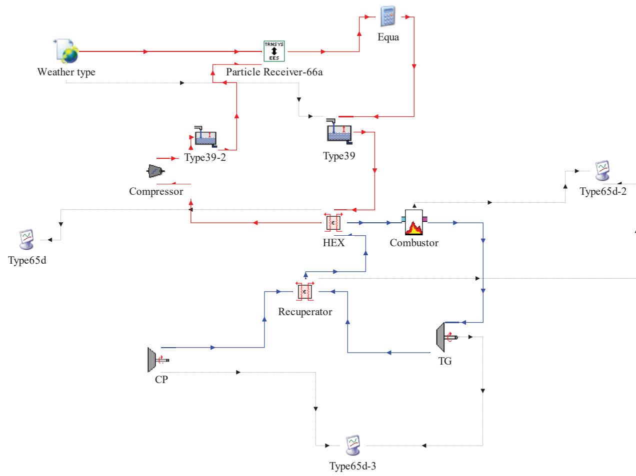

Figure 4. Simulation in TRNSYS.

Table 3. Comparison of present work with simulation in TRNSYS.

		Present work	TRNSYS	Relative error (%)
Input parameters	$\dot{m}\ (kg/s)$	17.5	17.5	----
	r_p	9.9	9.9	----
	η_{comp}	0.89	0.89	----
	η_{turb}	0.8	0.8	----
Output parameters	$T_2\ (°C)$	337	340	0.88
	$T_x\ (°C)$	555	520	6.7
	$T_z\ (°C)$	623	615	1.3
	$W_{GT}\ (MW)$	10.5	10.5	0.01
	$W_{comp}\ (MW)$	5.9	5.8	1.7
	$\eta_{Brayton}$	0.279	0.3	7

4 MULTI-OBJECTIVE OPTIMIZATION

The optimization algorithm used in this work is the elitist second-generation nondominated search genetic algorithm (NSGA-II). This algorithm has usually been implemented to optimize multi-objective problems because of their essential ability to escape from local optima, their extensibility in the multi-objective problems, and their ability to incorporate the handling of linear and nonlinear inequality and equality constraints in a straightforward way [21]. Any multi-objective optimization problem can be represented mathematically as follows:

$$MinF = Min(f_1(x), f_2(x) \dots f_n(x)) \quad s.t\ x \in X \tag{21}$$

Where $n \geq 2$ is the number of objective functions and X is the vector of decision variables. In this work, five decision variables, which are presented in Table 4, and two objective functions are defined: to maximize thermal efficiency and minimize fuel mass flow. NSGA-II algorithm was based on [22], which is an improved version of the NSGA algorithm [23], where the authors made an improvement to counter the computational complexity that NSGA had. In NSGA-II, the authors proposed to remove a shared parameter and replace it with a crowded comparison operator. This operator works as a selection guide for the nondominated solutions achieved by this algorithm producing an effective Pareto front.

https://doi.org/10.52202/077185-0129

Table 4. Magnitudes of the decision variables.

Variable	Lower value	Upper value
$T_1\ (°C)$	25	77
$P_1\ (MPa)$	7.4	8
$\dot{m}\ (kg/s)$	15	18
$T_3\ (°C)$	800	1177
r_p	2	6.5

In this work, the parameters used for optimization are a population size of 200 individuals, SBXCrossover of 95%, Polynomial mutation of $(1/\text{number of variables})$ and stop criterion of 10,000 iterations.

5 RESULTS

The NSGA-II algorithm used in this work was run 15 times to have a meaningful sample of the presented results**.** Python software and jMetalPy [24], which is written in its language, were used for optimization. Figure 5 shows the Pareto front of the optimization, where the thermal efficiency is maximized, and the fuel mass flow is minimized. The thermal efficiency varies from 17% to 40% and the mass flow from 0.107 to 0.196 kg/s. Since the algorithm is a metaheuristic, all the values reported in the Pareto front are optimal, therefore, a point must be chosen depending on the needs and characteristics of the problem under analysis. In this case, three points, A, B, and C, were taken. Point A is taken since it is the first value yielded by the optimization, point B is an intermediate point, and point C is the last point. The three points are compared, as well as with the non-optimized system, as shown in Table 5.

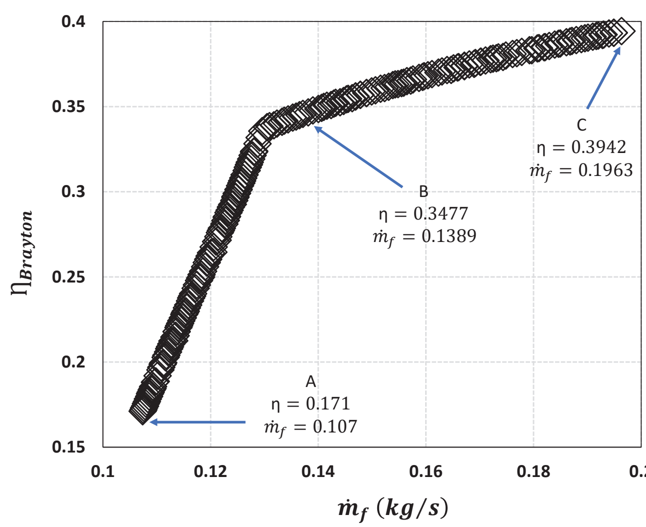

Figure 5. Pareto front of optimization.

Table 5 shows that the fuel mass flow decreased in the three optimized points compared to the non-optimized data: the variation ranges from 41% to 68% decrease. On the other hand, the thermal efficiency of the cycle has a better performance, concerning the non-optimized point, in points B and C. This increase is 13% and 30%, respectively. The net power generated by the cycle decreases in the

https://doi.org/10.52202/077185-0129

three optimized points as well as the residual heat, which can be used for a cogeneration cycle or hot water production.

To achieve this increase in thermal efficiency and decrease in fuel mass flow, Table 6 describes the values that the decision variables should take. Most of the variables of A, B, and C cases take the upper values imposed in Table 4. There is a considerable increase in the temperature T_1 until the upper limit or lower of the allowed range (see Table 4). This happens because of the supercritical CO_2 cycle, which needs at least a temperature of 31.5 °C and a pressure of 7.38MPa. In case these conditions are not fulfilled, the working fluid could be a two-phase mixture. On the other hand, it is appreciated that the mass flow of CO_2 decreased equally until the lower value of the allowed range (see Table 4) in the three optimized points. With respect to the temperature T_3, the inlet temperature of the gas turbine, there is a decrease in the A and B optimized points concerning the non-optimized one. This plays an important role in the reduction of fuel burning since a lower energy input is required to obtain these temperatures. Finally, an increment in the compression ratio, r_p, can be observed for points B and C, which translates into a greater difference in pressure and enthalpies.

Table 5. Comparison of optimized and non-optimized results.

	Non-optimized	**A**	**B**	**C**
$Pot_{Brayton}\ (MW)$	5.52	1.36	3.2	4.7
$\eta_{Brayton}$	0.3	0.17	0.34	0.39
$\dot{m}_f\ (kg/s)$	0.3394	0.1077	0.1396	0.1969
$\dot{Q}_h\ (MW)$	18.3	7.86	9.3	11.9
$\dot{Q}_L\ (MW)$	10.25	5.17	5.17	5.17
$W_{TG}\ (MW)$	5.97	1.8	4.7	6.2
$W_{CP}\ (MW)$	0.446	0.446	1.53	1.53

Table 6. Decision variables of non-optimized and optimized points.

	Non-optimized	**A**	**B**	**C**
$T_1\ (°C)$	25	77	77	77
$P_1\ (MPa)$	7.46	7.4	7.4	7.4
$\dot{m}\ (kg/s)$	17.9	15	15	15
$T_3\ (°C)$	1149	800	852	1177
r_p	4.5	2	6.5	6.5

6 CONCLUSIONS

The modeling and analysis of a solar-driven particle receiver system coupled with a supercritical carbon dioxide (CO_2) Brayton cycle is shown in this work. The particle receiver system requires the complex modeling of fluidized bed, thermodynamic properties, and heat transfer processes. Further, the power cycle model was described, including the compressor, gas turbine, and various heat exchangers. The particle receiver and the power cycle models were validated using Mathematica and TRNSYS 18 software, respectively. The results showed good agreement with the literature data, indicating the accuracy of the developed models. A multi-objective optimization was subsequently performed with the NSGA-II algorithm, which was used to maximize the thermal efficiency and minimize the fuel mass flow. The resulting Pareto front showed the trade-off between thermal efficiency and fuel mass flow.

https://doi.org/10.52202/077185-0129

Results from the optimization showed a significant decrease in fuel mass flow and a considerable improvement in thermal efficiency. Point B exhibits a 58.8% decrease in mass flow consumption compared to the non-optimized point. On the other hand, its thermal efficiency has increased by 13.3%. Point A, from the energetic point of view, is the worst performer. Point C has a 41.9% decrease in fuel mass flow with respect to the non-optimized point and a 30% increase in thermal efficiency. Therefore, the best points are points B and C. Another important aspect is the net power, all the optimized points suffer a decrease in power with respect to the non-optimized point. Point C has the highest net power with respect to the optimized points. This means that this point has more advantages over the others. Finally, concentrating solar power systems coupled to a power cycle offer a great advantage in producing electrical energy. On the other hand, metaheuristic optimization techniques show a good performance when applied to this type of system. The results show optimized operating points for a better performance of the power system.

NOMENCLATURE

T	Temperature	(°C)	k	Thermal conductivity	(W/mK)
P	Pressure	(MPa)	ρ	Density	(kg/m^3)
$\dot{Q}$	Heat transfer rate	(MW)			
$\dot{W}$	Work	(MW)			
$\dot{m}$	Mass flow rate	(kg/s)			

Subscript

DPS	Dense Particle Suspension	t	Tube
f	Fuel	p	Particle
LHV	Low Heating Value	g	gas

REFERENCES

[1] G. Flamant *et al.*, "Dense suspension of solid particles as a new heat transfer fluid for concentrated solar thermal plants: On-sun proof of concept," *Chem Eng Sci*, vol. 102, pp. 567–576, Oct. 2013, doi: 10.1016/j.ces.2013.08.051.

[2] I. Perez Lopez *et al.*, "On-sun operation of a 150 kWth pilot solar receiver using dense particle suspension as heat transfer fluid," *Solar Energy*, vol. 137, pp. 463–476, Nov. 2016, doi: 10.1016/j.solener.2016.08.034.

[3] H. Zhang, H. Benoit, I. Perez-Lopèz, G. Flamant, T. Tan, and J. Baeyens, "High-efficiency solar power towers using particle suspensions as heat carrier in the receiver and in the thermal energy storage," *Renew Energy*, vol. 111, pp. 438–446, 2017, doi: 10.1016/j.renene.2017.03.101.

[4] S. Wang, K. Luo, C. Hu, J. Lin, and J. Fan, "CFD-DEM simulation of heat transfer in fluidized beds: Model verification, validation, and application," *Chem Eng Sci*, vol. 197, pp. 280–295, Apr. 2019, doi: 10.1016/j.ces.2018.12.031.

[5] R. Hay and K. Celik, "Accelerated carbonation of reactive magnesium oxide cement (RMC)-based composite with supercritical carbon dioxide (scCO2)," *J Clean Prod*, vol. 248, Mar. 2020, doi: 10.1016/j.jclepro.2019.119282.

[6] P. Sharan, T. Neises, and C. Turchi, "Optimal feed flow sequence for multi-effect distillation system integrated with supercritical carbon dioxide Brayton cycle for seawater desalination," *J Clean Prod*, vol. 196, pp. 889–901, Sep. 2018, doi: 10.1016/j.jclepro.2018.06.009.

[7] Z. Liu, X. Cao, T. Wang, W. Jia, and Z. Duan, "Comparative evaluation of the refrigeration compressor performance under different valve parameters in a trans-critical CO 2 cycle," *International Journal of Refrigeration*, vol. 101, pp. 34–46, May 2019, doi: 10.1016/j.ijrefrig.2019.02.034.

 https://doi.org/10.52202/077185-0129

[8] Y. Ahn *et al.*, "Review of supercritical CO2 power cycle technology and current status of research and development," *Nuclear Engineering and Technology*, vol. 47, no. 6. Korean Nuclear Society, pp. 647–661, Oct. 01, 2015. doi: 10.1016/j.net.2015.06.009.
[9] S. Khatoon and M. H. Kim, "Preliminary design and assessment of concentrated solar power plant using supercritical carbon dioxide Brayton cycles," *Energy Convers Manag*, vol. 252, Jan. 2022, doi: 10.1016/j.enconman.2021.115066.
[10] E. Guelpa and V. Verda, "Exergoeconomic analysis for the design improvement of supercritical CO2 cycle in concentrated solar plant," *Energy*, vol. 206, Sep. 2020, doi: 10.1016/j.energy.2020.118024.
[11] A. Gallo, J. Spelling, M. Romero, and J. González-Aguilar, "Preliminary Design and Performance Analysis of a Multi-megawatt Scale Dense Particle Suspension Receiver," in *Energy Procedia*, Elsevier Ltd, May 2015, pp. 388–397. doi: 10.1016/j.egypro.2015.03.045.
[12] J. I. Córcoles, M. Díaz-Heras, M. Fernández-Torrijos, and J. A. Almendros-Ibáñez, "Flow and heat transfer analysis of a gas–particle fluidized dense suspension in a tube for CSP applications," *Renew Energy*, vol. 206, pp. 1–12, Apr. 2023, doi: 10.1016/J.RENENE.2023.02.004.
[13] Inc. Wolfram Research, "Mathematica, Version 13.2." Champaign, IL, 2023.
[14] M. A. Reyes-Belmonte, A. Sebastián, J. Spelling, M. Romero, and J. González-Aguilar, "Annual performance of subcritical Rankine cycle coupled to an innovative particle receiver solar power plant," *Renew Energy*, vol. 130, pp. 786–795, Jan. 2019, doi: 10.1016/j.renene.2018.06.109.
[15] O. Molerus and K.-E. Wirth, *Heat Transfer in Fluidized Beds*, Springer. Dordrecht: Springer Netherlands, 1997. doi: 10.1007/978-94-011-5842-8.
[16] Wen-Ching Yang, *Handbook of Fluidization and Fluid-Particle Systems*. CRC Press, 2003. Accessed: Jan. 31, 2024.
[17] M. Leva and M.Grummer, "A correlation of solids turnover in fluidized systemsits relation to heat transfer," *Chem Eng Prog*, vol. 48, pp. 307–313, 1952.
[18] D. Olivenza-León, A. Medina, and A. Calvo Hernández, "Thermodynamic modeling of a hybrid solar gas-turbine power plant," *Energy Convers Manag*, vol. 93, pp. 435–447, Mar. 2015, doi: 10.1016/j.enconman.2015.01.027.
[19] S. A. Klein, "Trnsys." 2018. Accessed: Jan. 31, 2024. [Online]. Available: http://www.trnsys.com/
[20] S. A. Klein, "Engineering equation solver ´(EES) v10.64." 2019. Accessed: Jan. 31, 2024. [Online]. Available: http://fchartsoftware.com/ees/
[21] I. Giagkiozis, R. C. Purshouse, and P. J. Fleming, "An overview of population-based algorithms for multi-objective optimisation," *International Journal of Systems Science*, vol. 46, no. 9. Taylor and Francis Ltd., pp. 1572–1599, Jul. 04, 2015. doi: 10.1080/00207721.2013.823526.
[22] K. Deb, A. Pratap, S. Agarwal, and T. Meyarivan, "A Fast and Elitist Multiobjective Genetic Algorithm: NSGA-II," 2002.
[23] N. Siinivas and K. Deb, "Multiobjective Optimization Using Nondominated Sorting in Genetic Algorithms," *Evol Comput*, vol. 2, no. 3, pp. 221–248, 1995.
[24] A. Benítez-Hidalgo, A. J. Nebro, J. García-Nieto, I. Oregi, and J. Del Ser, "jMetalPy: A Python framework for multi-objective optimization with metaheuristics," *Swarm Evol Comput*, vol. 51, Dec. 2019, doi: 10.1016/j.swevo.2019.100598.

ACKNOWLEDGEMENT

J.A Moctezuma-Hernandez acknowledges financial support from CONAHCYT.

https://doi.org/10.52202/077185-0129